https://doi.org/10.1088/1361-665X/ac08ae

Experimentally verified finite element modeling and analysis of a conformable piezoelectric sensor

Nikta Amiri¹, Farita Tasnim², Mostafa Tavakkoli Anbarani¹, Canan Dagdeviren^{2,*}
and M Amin Karami^{1,*}

E-mail: karami@buffalo.edu and canand@media.mit.edu

Received 20 December 2020, revised 15 April 2021 Accepted for publication 4 June 2021 Published 25 June 2021



Abstract

This paper presents development of a three dimensional finite element model for simulations of a conformable piezoelectric sensor utilizing COMSOL Multiphysics. The sensor has a multi-layer structure composed of four circular piezoelectric elements arranged in an array structure laminated on a soft substrate and is capable of providing a strain mapping of soft tissue surfaces for spatiotemporal biokinematic assessment of the facial skin. Here, we provide the finite element method (FEM) for the sensor to predict its electromechanical behavior. This paper studies the effect of the design parameters such as dimensions of the piezoelectric sensor and the substrate on voltage sensitivity and sensor compliance. The FEM model is established to understand the underlying physics and guide the mechanical characterization of the system. The developed model is experimentally verified through two series of tests. The first set of tests involve comprehensive *in vitro* mechanical testing to provide accurate measurements of strain during compression, stretching, and bending. The second set of tests present *in vivo* experiments on healthy and amyotrophic lateral sclerosis subjects. The experimentally verified FEM model provides a detailed insight into analyzing the response of the sensor which establishes new design rules for next generations of conformable piezoelectric sensors.

Supplementary material for this article is available online

Keywords: finite element method, conformable piezoelectric sensor, design, optimization, skin sensor

(Some figures may appear in colour only in the online journal)

1. Introduction

In recent years, conformable piezoelectric sensors have emerged for biomedical purposes for which wearable or skinattachable devices could allow seamless integration with curvilinear soft substrates, continuous monitoring of human body parts, and an improved user experience [1]. The ultrathin architectures of the active elements yield low modulus, stretchable mechanics when supported by a thin elastomer [2, 3]. Some striking examples incorporate lead zirconate titanate (PZT) ribbons for *in-vivo* measurements of skin properties to provide a noninvasive approach of assessing the skin mechanical properties [4–7]. Other piezoelectrically driven systems are based on another polymer piezoelectric material, polyvinylidene fluoride (PVDF), which is in coherence with human skin for a wide range of biomedical purposes such as pulse monitoring [8, 9], thermal sensing

¹ Department of Mechanical and Aerospace Engineering, University at Buffalo (SUNY), Buffalo, NY 14260, United States of America

² Media Lab, Massachusetts Institute of Technology, Cambridge, MA 02139, United States of America

^{*} Author to whom any correspondence should be addressed.

[10, 11], and physiological signal monitoring on the human wrist [12].

Comprehensive studies of conformable piezoelectric systems are typically done through experiments along with analytical [13-20] and numerical [21, 22] methods to model and analyze the response of the system. The finite element method (FEM) method is advantageous over the analytical methods since it can accommodate all of the details of multilayered complex sensors. In a fabricated skin-mounted sensor for measuring arterial pulse wave pressure, the FEM model has been used to evaluate deformation mechanism under uniaxial compression and confirm the relation between voltage and compression [3, 23]. Piezoelectric transducers based on macro fibre composites (MFCs) are also used for energy harvesting [24, 25], actuation [26–29] and sensing [30, 31]. FEM modeling in COMSOL Multiphysics has been proposed to numerically evaluate the equivalent properties of MFC consisting of PZT fibers embedded in an epoxy matrix [32–34]. The numerical method has been implemented to analyze the responses of piezoelectric actuators used in synthetic jet devices, and the results have been further validated with experimental data and analytical results [35]. In the design of wavy PZT nanoribbons integrated with soft, elastomeric support of PDMS, a FEM using Abaqus has been performed to determine the buckling deformation at the edges of the ribbons [36]. The buckled PVDF fibers on PDMS substrate were simulated using commercial finite element analysis software Abaqus to assess buckling modes of PVDF nanofibers with different width to height aspect ratio [37]. The effect of geometrical design parameters on the performance of a tactile sensor composed of PVDF piezoelectric film integrated with PDMS polymer vertical fiber has been analyzed using FEM [38].

In a recent study, precise measurements of soft tissue biokinematics via conformable piezoelectric sensor have been used to computationally recognize distinct facial motions, and thus facilitate nonverbal communication for patients who lack the ability to speak or interact with traditional electronic communication interfaces [39].

Here, we report comprehensive FEM analysis of this conformable sensor that can translate patterns of facial soft tissue biomechanics in vivo into interpretable electrical signals to enable new forms of non-verbal communication. The design, characterization and validation methods to be introduced in this paper offer new routes for rapid, in vivo bio kinematic assessment of epidermal surfaces during dynamic movements. The FEM model is developed and validated first against a series of controlled experiments. These control experiments include subjecting the conformable sensor to axial, tensile, and compressive loads and loads along the thickness direction. We also verify our FEM model during human trials, by measuring the strain at the surface of the conformable Facial Code Extrapolation Sensor (cFaCES) and the voltage generated by it and comparing it with the results of the model. Our high fidelity fully coupled dynamic models allow us to perform a detailed parametric study to identify the most optimal device configuration. It also allows us to understand interesting phenomena happening during the human trials (for example the discrepancy between the skin strain and the strain measured using stereophotogrammetry see section 4). The paper is organized as follows. The details of the proposed model including material properties and fabrication steps are described in section 2. The FEM is then validated with experiments in section 3. The analytic model, which accounts for the interaction between the sensor and the facial skin, and strain distribution in different layers of sensor using the FEM model is discussed in detail in section 4. Section 5 describes design considerations including minimum radius of curvature requirement and effect of shape on sensor stiffness. Section 6 presents a strategy to conduct parametric studies and optimization for the effect of geometric properties on sensor performance. The paper concludes with some summary remarks in section 7.

2. Device configuration, microfabrication steps, and modeling

To offer a system capable of characterizing facial motions, we design and develop a cFaCES. The sensor consists of aluminum nitride (AlN) piezoelectric thin films on a skin-like polydimethylsiloxane (PDMS) substrate. AlN is used as the piezoelectric material in cFaCES for several reasons: it is a relatively low cost material with a lead free nature which makes it suitable for mass production, smooth clinical transition, and adoption in future lead-free industrial standards. Furthermore, it has complementary metal oxide semiconductor (CMOS)compatible processing; however, standard thin film piezoelectrics such as PZT is not CMOS-compatible and may suffer from aging and other material property changes over time. The complaint substrate with low elastic modulus close to human epidermis enables seamless integration of the sensor with facial skin. Figure 1(a) shows the schematic diagram of a cFaCES. The sensor has multi-layer, ultra-thin architecture and is supported by a thin elastomer (PDMS, 40 μ m thick) substrate. The cFaCES consists of an array of four circular thin films (1.5 μ m thick, 0.48 cm diameter) sandwiched between two Molybdenum (Mo) electrodes (200 nm thick) and encapsulated with a 1 μ m thick layer of silicon dioxide (SiO₂). Molybdenum provides good adhesion as electrode material for the AlN layer by offering lower epitaxial strain at the interface. The four sensing elements are not connected neither in series nor in parallel, and each element is separate. The circular shape of piezoelectric elements allows for eliminating directional bias in localized spatiotemporal strain measurements. Circular coordinate system is axisymmetric which eliminates the directional bias. The circular geometry allows the strain to be uniformly distributed across the surface, while square geometry for piezo elements results in strain concentration at the sharp corners. The piezoelectric elements have the simplified structure of 2×2 arrays with the same center to center distance (0.6 cm) between the elements in x and y

The mechanical and geometric properties of each layer are displayed in table 1.

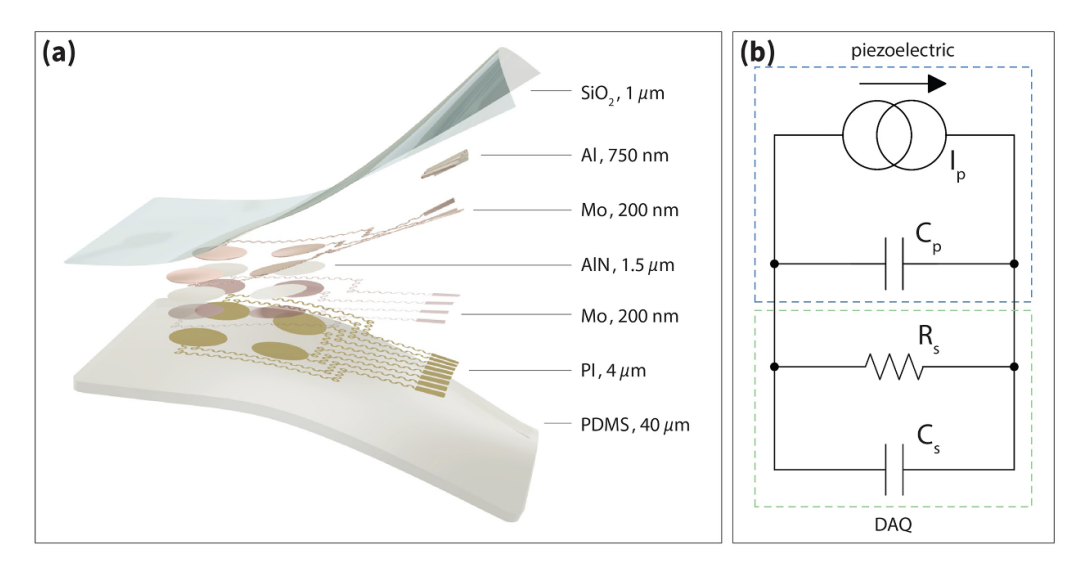


Figure 1. (a) Exploded view of the conformable sensor. The device consists of a substrate layer of PDMS, a bottom encapsulation layer of polyimide (PI), a bottom electrode of molybdenum (Mo), a piezoelectric layer of AlN, a top electrode of Mo, bonding pads of aluminum (Al), and a final top encapsulation layer of silicon dioxide (SiO₂). The eight electrical lines show the sensing elements are not connected and each element is separate. (b) Simplified circuit diagram of a single sensing element (blue dashed box) as a current source I_p in parallel with a capacitor $C_p = 807 \, \text{pF}$, which mimics the piezoelectric charge-generating behavior. In order to accurately predict the voltage values measured from the sensor, the data acquisition (DAQ) system (green dashed box) is included in the model as a parallel combination of a resistor and capacitor ($R_S = 1 \, \text{M}\Omega \parallel C_S = 265 \, \text{pF}$) connected to the two-wire output of the piezoelectric element.

Table 1. Mechanical and geometric properties of each layer to calculate the neutral mechanical plane.

Layer	Young's modulus (E) (Pa)	Poisson's ratio (ν) (1)	Area (A) (m ²)	Thickness (th) (m)	Distance from bottom to the middle of layer (h) (m)
PDMS	7.5×10^{5}	0.49	7.0×10^{-4}	40×10^{-6}	2.00×10^{-5}
PI	3.1×10^{9}	0.34	7.2×10^{-5}	4×10^{-6}	4.20×10^{-5}
Bottom Mo	3.12×10^{11}	0.31	7.2×10^{-5}	0.2×10^{-6}	4.41×10^{-5}
AlN	3.89×10^{11}	0.23	7.2×10^{-5}	1.5×10^{-6}	4.50×10^{-5}
Top Mo	3.12×10^{11}	0.31	7.2×10^{-5}	0.2×10^{-6}	4.58×10^{-5}
SiO_2	7.0×10^{10}	0.17	7.0×10^{-4}	1×10^{-6}	4.64×10^{-5}

In such a multi-layer structure, the location of the neutral mechanical plane (NMP) is calculated as:

$$y_{\text{NA}} = \frac{\sum_{i=1}^{n} \overline{E_i} A_i h_i \left[\left(\sum_{j=1}^{i} h_j \right) - \frac{h_i}{2} \right]}{\sum_{i=1}^{n} \overline{E_i} A_i h_i}$$
(1)

$$\overline{E_i} = E_i \left(1 - v_i^2 \right) \tag{2}$$

Where E_i , $\overline{E_i}$, v_i , A_i , h_i are the plane-strain modulus, modulus of elasticity, poisson's ratio, area and thickness of the *i*th layer, respectively (i=1 represents the bottom layer (PDMS) and i=5 represents the top layer (SiO₂)). The location of the neutral mechanical plane is calculated as 600 nm of the midplane of the piezoelectric active layer based on equations (1) and (2) [39].

The microfabrication of a cFaCES starts from a standard wafer cleaning process on an 8 inch silicon (Si) test wafer (Sumco Corp., Tokyo, Japan). Subsequently, a layer of 50 nm thick Al was deposited on the surface of the cleaned

Si wafer. Using plasma-enhanced chemical vapor deposition (PE-CVD, Oxford Instruments, Bristol, UK), a silicon dioxide layer was grown on the Si wafer with the following precursors: SiH4 (260 sccm), N2O (1000 sccm) and N2 (500 sccm). Mo bottom electrode (200 nm thick) has been deposited onto the soft oxide layer by sputtering technique in the same deposition run, followed by an AlN bulk layer deposition (1.5 μ m thick). Both AlN seed and bulk layers have been deposited using a pure Al target (99.9995%, Vacuum Engineering & Materials Co. Santa Clara, CA, USA) in a mixture of Ar (20 sccm) and N2 (20 sccm) gases in direct current (DC) pulsed power supply (Sigma Deposition Systems, SPTS Technologies, Newport, UK) at 750 W and with a working pressure of 2.8×10^{-3} mbar. Mo layer has been sputtered using a pure Mo target (99.95%, Vacuum Engineering & Materials Co. Santa Clara, CA, USA) in pure Ar atmosphere (66 sccm) under DC power supply of 400 W and a working pressure of 5×10^{-3} mbar. After the optical lithographic process to pattern AlN and Mo stacked layers, the Mo top layer was sputtered in the same condition of the Mo bottom electrode layer. The Mo top layer was dry etched by an inductively

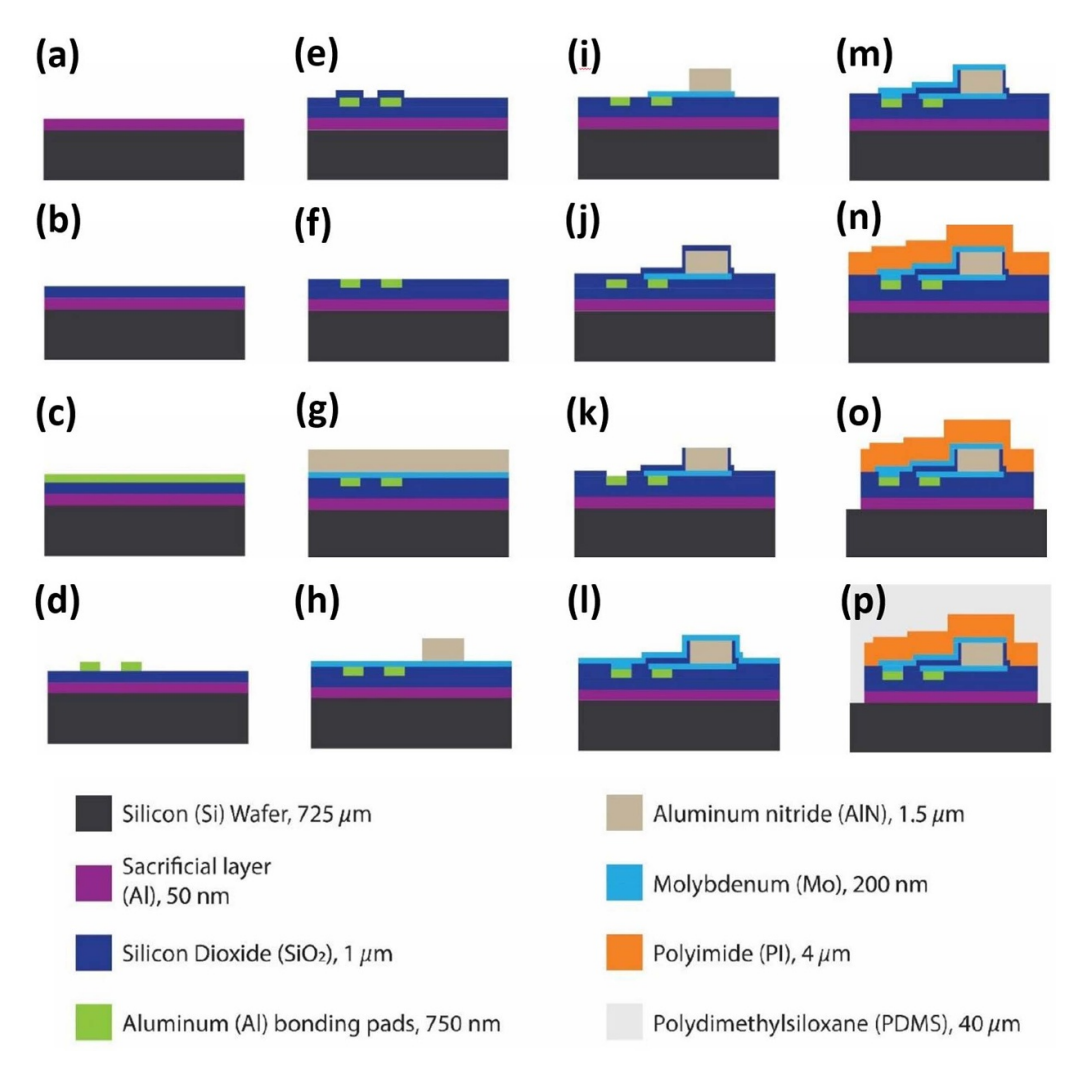


Figure 2. Microfabrication steps for cFaCES. Each step of microfabrication of a cFaCES is represented by a depiction of the cross section of the device after that step. (a) Deposition of sacrificial layer onto surface of cleaned Si wafer. (b) Growth of SiO₂ layer using PECVD. (c) Deposition of aluminum layer and (d) patterning to create bonding pads. (e) Continued growth of SiO₂ layer using PECVD. (f) Grinding of SiO₂ layer to desired thickness. (g) Sputtering of Mo electrode and of AlN layers. (h) Patterning of AlN layers. (i) Patterning of Mo electrode. (j) Growth and (k) patterning of oxide insulating layers. (l) Sputtering and (m) patterning of Mo electrode. (n) Spin-coating and (o) patterning of PI encapsulation layer. (p) Spin-coating PDMS to create an encapsulation layer. Subsequent anodization releases the final cFaCES device from the substrate, after which bonding pads are exposed by patterning the SiO₂ layer. Figure not to scale.

coupled plasma (ICP)-reactive ion etching system (PlasmaPro 100 Cobra ICP etching system, Oxford Instruments, Abingdon, UK) under the same conditions reported for the Mo bottom layer. Eventually, PI2611 PI precursor solution (HD Microsystems, Parlin, NJ, USA) was spin coated (PWM50, Headway Research, Inc. Garland, TX, USA) at 2000 rpm for 60 s on the Mo top electrode and followed by a curing process at 350 °C for 30 min performed on a VWR® hot plate (VWR International, Radnor, PA, USA). Then, a layer of polydimethylsiloxane (PDMS, matrix/crosslink ratio 1:10), SylgardTM 184 Silicone Elastomer, Electron Microscopy Science) was spin coated (1000 rpm, 60 s) and cured at 60 °C overnight in a curebox (CB-4015, Wicked Engineering, USA) as the final encapsulation layer. Each step of microfabrication is shown in detail in figure 2.

To study the behavior of the sensor, we develop finite element analysis simulations through COMSOL Multiphysics. The accuracy of our FEM is confirmed with the experimental

mechanical test results from well-behaved, periodic voltage output of the system. The sensor is coupled with 2 mm thick mock skin (Dragon Skin 30, Smooth-On, Inc., Macungle, United States) and dynamically loaded under compression, bending, and stretching for mechanical characterization of the system. The FEM is also extended to explore the effects of various geometrical parameters on sensor performance, so as to work toward optimization of the sensor design. The physics in the FEM is composed of three coupled interfaces including Solid Mechanics, Electrostatics, and Electrical Circuits in COMSOL Multiphysics Version 5.4. Constitutive relations of piezoelectric material properties are defined as:

$$D = dT + \varepsilon^T E \tag{3}$$

$$S = s^E T + dE \tag{4}$$

Compliance matrix (Pa ⁻¹) Coupling matrix (C N ⁻¹) Electric permittivity (F m ⁻¹) s_{11} 2.89×10^{-12} d_{31} -1.91×10^{-12} ε_{11} 8.15×10^{-11} s_{12} -9.32×10^{-12} d_{32} -1.91×10^{-12} ε_{22} 8.15×10^{-11} s_{13} -5.00×10^{-12} d_{33} 4.95×10^{-12} ε_{33} 8.96×10^{-11} s_{22} 2.89×10^{-12} d_{15} -3.84×10^{-12} ε_{22} s_{23}	$\begin{array}{cccccccccccccccccccccccccccccccccccc$						
$\begin{array}{cccccccccccccccccccccccccccccccccccc$	$\begin{array}{cccccccccccccccccccccccccccccccccccc$	Compliance matrix (Pa ⁻¹)		Coupling matrix (C N ⁻¹)		Electric permittivity (F m ⁻¹)	
	s_{33}	s_{12} s_{13} s_{22}	$-9.32 \times 10^{-12} -5.00 \times 10^{-12} 2.89 \times 10^{-12}$	$d_{32} \\ d_{33} \\ d_{15}$	-1.91×10^{-12} 4.95×10^{-12} -3.84×10^{-12}	$arepsilon_{22}$	8.15×10^{-11}

Table 2. Electrical properties of aluminum nitride.

where D represents the electric displacement, T the stress, E the electric field, d the piezoelectric constant, ε^T the permittivity at constant stress, S the strain, and s^E the compliance coefficient measured at a constant electric field. The electrical properties of the sensing elements are displayed in table 2.

In solid mechanics interface, mechanical properties of materials are described as linear elastic with solid isotropic model and equations for time dependent study are defined as

$$S = C : \epsilon, \tag{5}$$

$$S = C(E, v) \tag{6}$$

The dynamic equation of motion is

$$\rho \frac{\partial^2 u}{\partial t^2} = \nabla . S$$

where S is stress matrix, C is elastic stiffness tensor which is function of young's modulus (E) and poisson's ratio (ν), ϵ is strain tensor, u is displacement field vector, and ρ is density. Displacement field vector u is related to strain tensor ϵ with the equation $\epsilon = \frac{1}{2} \left(\nabla u + \nabla u^T \right)$. The bottom surfaces of piezoelectric elements are grounded with V=0 in time dependent study, and the top surfaces are defined as terminals with equations $\int D.n \, dS = Q_0 \frac{\partial Q_0}{\partial t} = I_{cir}$, where D is the vector of electric displacement, n is the unit outward normal, Q_0 is charge stored in the capacitor, and I_{cir} is the circuit current. Then, the terminals are coupled with an electrical circuit interface composed of external terminals as parallel combination of a resistor and capacitance ($R = 1 \text{M}\Omega \parallel C = 265 \, \text{pF}$). The external circuit is shown in figure 1(b) in a green dashed box connected to piezo elements in parallel to model the data acquisition system (DAQ). One single sensing element, blue dashed box in figure 1(b), acts as a current source in parallel with a capacitor, which mimics the piezoelectric chargegenerating behavior. The schematic in figure 1(b) is a simplified illustration to emphasize that all derived modes in charge calculation and backwards coupling are considered in the model. The internal capacitance is calculated as 807 pF from the equation

$$C_{\text{piezo}} = \frac{A \,\varepsilon_0 \,\varepsilon_r}{d}$$

where A is area of piezo element, ε_0 is permittivity of air, ε_r is relative permittivity, and d is the thickness of the piezo element. The geometry is discretized with swept meshing which

is the most effective way to model the geometries with high aspect ratio. The sensor is composed of ultra thin layers and swept meshing creates far less mesh elements in thickness direction and avoids overabundance of elements for a thin geometry. However, other meshing techniques like hexahedral or prismatic meshing are not suitable for disproportionate dimension sizes, since they create the same amount of elements in all directions [40].

3. Mechanical characterization

To experimentally verify the finite element model, we perform a series of mechanical tests. We subject the sensor to different load profiles including bending, axial stretching, and compression in the thickness direction. We conduct mechanical tests with the sensor adhered to a 2 mm thick mock skin (Dragon Skin 30, Smooth-On, Inc., Macungle, United States). Experimental tests of the mechanical performance of the piezoelectric sensor (figure 4) were performed using a micro universal testing system (MicroTester 5948, Instron, Norwood, United States) equipped with a 50 N load cell exhibiting the force resolution of 2 mN. During the mechanical tests, the cFaCES was electrically connected with a DAQ system with PXIe-1071, PXIe-8821 and PXIe-4464 components (National Instruments, Austin, TX, United States). The electrical output (voltage) from the cFaCES was recorded in real time with application of a 6th order Butterworth filter, since a 6th order filter has a good combination of signal integrity and noise reduction as well as a good signal to noise ratio compared to the other filters. Electrical data was recorded with NI SignalExpress 2015 and mechanical data was recorded in Blue-Hill software. Cycles of compression (200 \times), bending (50 \times) and stretching $(20\times)$ were conducted for each type of testing, respectively. Bending and stretching mechanical tests were performed using cyclic displacement profiles, and for compression tests, force profile was used instead of displacement profiles.

The system is composed of a multi-layer sensor laminated on a 2 mm \times 2.5 cm \times 9 cm mock skin (Dragon Skin 30, Smooth-On, Inc., Macungle, United States) such that the middle of the sensing elements array (green dashed line) is located in the middle of the sensor-mock skin structure in the x-y plane as shown in figure 3. Each end of the mock skin substrate is 1.8 cm long which leaves a testing length of 5.4 cm.

In stretching and bending tests, one end of mock skin is clamped and the other end is either moving towards or moving away from the clamped side, resulting in bending and stretching respectively. Then it is released and the structure

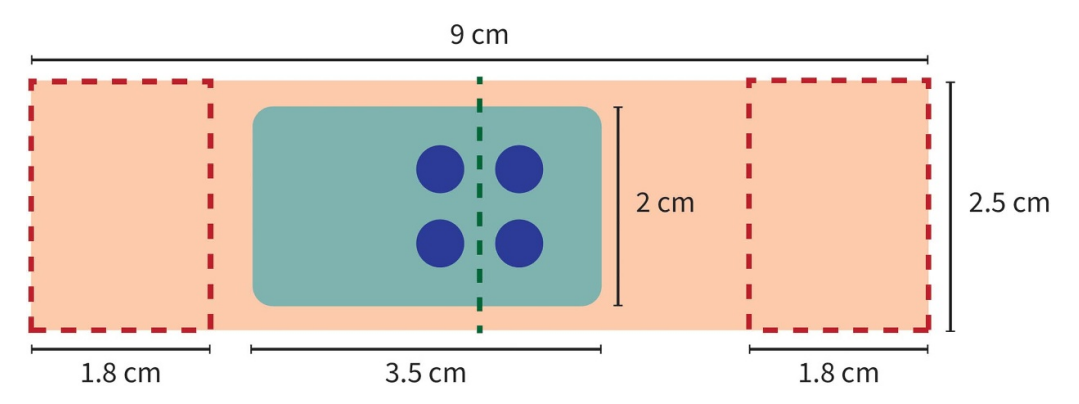


Figure 3. Schematic of the cFaCES coupled with mock skin geometrical configuration as utilized in mechanical testing. The exposed area of the mock skin is represented by the orange box minus the regions (two dashed red boxes) where the Instron clamps onto the mock skin. The cFaCES is aligned on the mock skin such that the middle of the cFaCES sensing elements (green dashed line) is aligned with the middle of the exposed area of the mock skin.

returns back to its original location. The motion is cyclically repeated with 0.5 Hz frequency for 10 s. In compressive test, the bottom surface of the sensor is placed on a flat horizontal surface, and the top surface is free. The compressive load is applied on top of the sensor by exciting harmonic mechanical loads. The motion is cyclically repeated with 0.2 Hz frequency for 100 s. Figure 4(a) shows the instant of maximum displacement for bending, stretching, and compression state. Figure 4(b) illustrates the displacement and strain profile coming from the developed FEM model. In bending and stretching tests, the clamped end has zero displacement shown in blue, and the free end reaches the maximum displacement of 3.5 mm in stretching and 10 mm in bending shown in red. By looking at the videos of the stretching tests we noticed that the beams indeed slip out of the jaw during the 'stretching' tests. The main reasons for the slippage of the beam in the first cycle is (a) the prescribed axial deformation was too much, inducing large axial force and (b) the beam is so thin and could slide out of the jaws under large tensile forces. To be conformable, the piezoelectric element in the cFaCES is very thin. This gives the sensor very small bending stiffness. As a result, the sensor easily buckles under axial stiffness. This sensitivity to buckling caused the specimen to exhibit buckling during the tests that were intended for stretching (available online at stacks.iop.org/SMS/30/085017/mmedia). In compression tests, all over the surface area of the sensor is compressed uniformly, and the displacement is almost uniform of 2 mm at the instant of maximum displacement.

In all tests, the strain in piezo elements is significantly lower than the rest of the surface since the piezo stiffness is three orders of magnitude higher than other elements (maximum strain of 0.13% in bending and 0.0076% in stretching). Figure 4(c) shows the input to the cFaCES displacement profile with a maximum of 3.5 mm in stretching, a maximum of 10 mm in bending, and loading profile with a maximum of 1.9 N. Figure 4(d) illustrates the voltage output from both the FEM model and the experiments. The peak voltage output from the model is 6.7 mV in bending, 5 mV in stretching, and 3.5 mV in compression. The FEM results are in agreement with the experiments and validate the accuracy of the model.

4. Human subject trials

In this section, we first develop an analytical model to predict the principal strains from the measured voltages during in vivo trials. The sensor is laminated over the face of a healthy subject, and the subject performs facial motions of either vocal, eyebrow, or cheek motion as shown in figure 5.

The principal strain and generated voltage are measured. The FEM model is further utilized to analyze the strain distribution over the sensor surface and along different layers to investigate the physics of the device. We can write the following expression based on the constitutive equation of the piezoelectric material when there is dominant stress in radial directions. The equation describes the relation between voltage output of the sensor and the strain occurring on the skin underneath assuming the strain is uniform over the area of each circular sensing element [41, 42]:

$$C\frac{\mathrm{d}V}{\mathrm{d}t} + \frac{V}{R} = e_{31}A\frac{\mathrm{d}\left(\epsilon_1 + \epsilon_2\right)}{\mathrm{d}t} \tag{7}$$

where C is the capacitance of the sensor, R is the shunt resistance of the DAQ, e_{31} is the effective piezoelectric stress coefficient coming from the FEM model, A is the area of the piezoelectric elements, ϵ_1 and ϵ_2 are two principal strain directions. During some facial motions, wrinkle lines appear which indicate non zero shear strains. However, shear strains do not induce any piezoelectric response, since the coupling coefficient between the shear strain in the X-Y plane and the electrodes in the Z axis is zero, and. The generated voltage correlates with some of principal strains represented as $\epsilon_1 + \epsilon_2$ and ϵ_3 is assumed negligible. Equation (7) in frequency domain ϵ_3 is assumed negligible. Equation (7) in frequency domain is written as: $Cj\omega + \frac{V}{R} = e_{31}A \ (\epsilon_1 + \epsilon_2) j\omega$. Rearranging the equation in frequency domain results in the following transfer function $\frac{(\epsilon_1 + \epsilon_2)(\omega)}{V(\omega)} = \frac{1}{Re_{31}Aj\omega} + \frac{C}{e_{31}A}$. Since, the term $\frac{C}{e_{31}A}$ is negligible compared to the term $\frac{1}{Re_{31}Aj\omega}$, we can obtain the simplified transfer function between the principal strains and the generated voltage as $\frac{(\epsilon_1 + \epsilon_2)(\omega)}{V(\omega)} = \frac{1}{Re_{31}Aj\omega}$. On each column of figure 6, three plots of generated voltage approximate approximate prodicted strains from

voltage captured from the experiment, predicted strains from

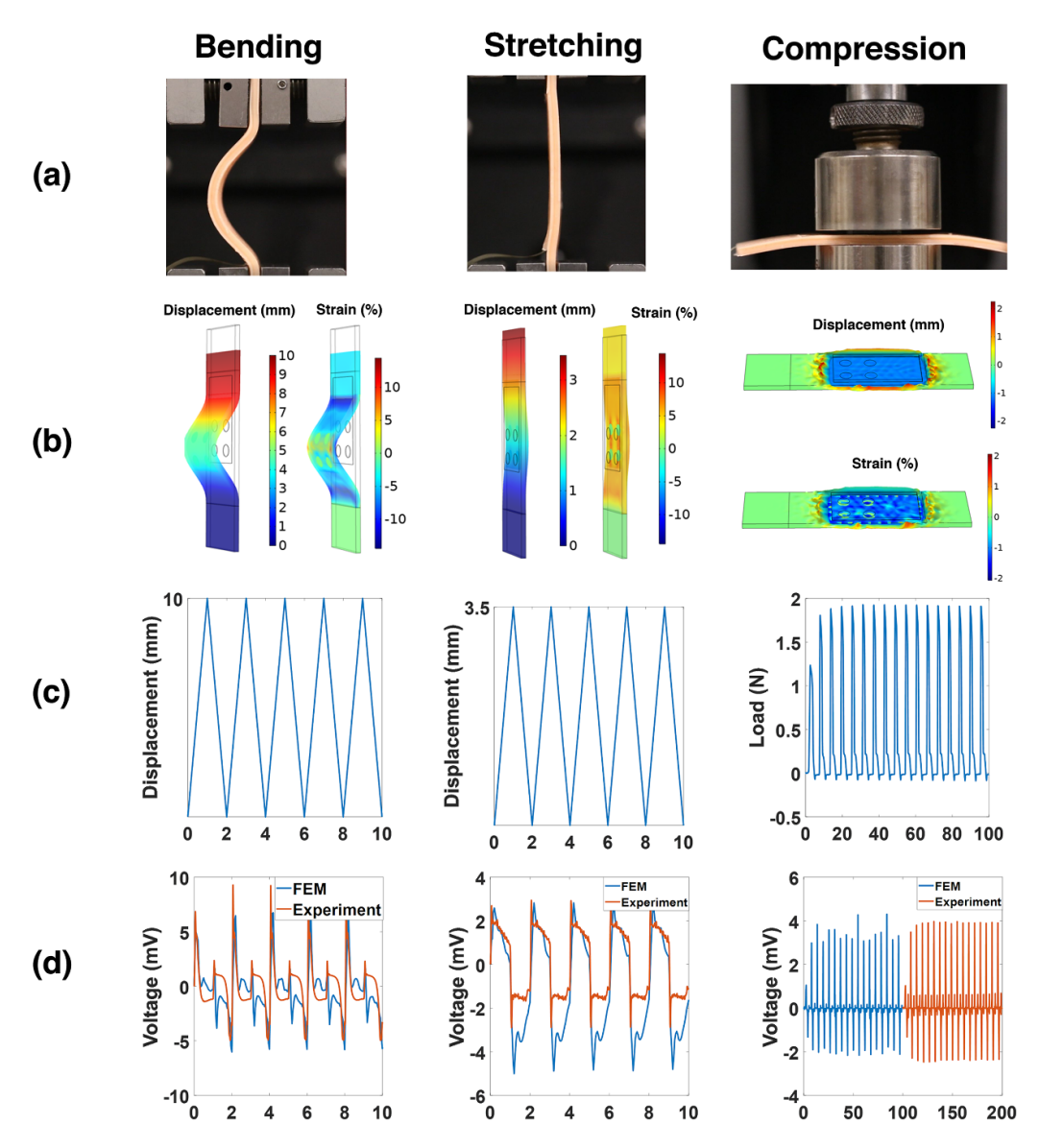


Figure 4. Mechanical characterization of the cFaCES. (a) The experimental setup on the Instron machine the top end of the Instron stage is either pushed closer, resulting in buckling behavior, or pulled away, resulting in tensile stretching behavior, or loaded along thickness resulting in compression. (b) Displacement map coming from the FEM model for the instant of maximum displacement. The buckled state with 10 mm displacement, the stretched state with 3.5 mm displacement, and the compression test with maximum force of 1 N. (c) Periodic voltage output from FEM and experiment. All *x*-axes are time in seconds.



Figure 5. The cFaCES adhered to the facial skin, on the temple or cheek, of four different human subjects.

the FEM model, and measured experimental strains are displayed. While strain magnitudes coming from the model are smaller than the experiments, there is good qualitative agreement for different facial motions (the difference in the voltage magnitude is discussed in details later in this section). This close qualitative match validates the model to predict the strain

shape based on voltage performance of the sensor laminated on the human facial skin. Although the experimental graphs in figure 6(b) look qualitatively the same as graphs in figure 6(c), the DIC measured strains are higher in magnitude than the estimated strains at the piezoelectric patches. The discrepancy between quantitative strain values can be attributed to the

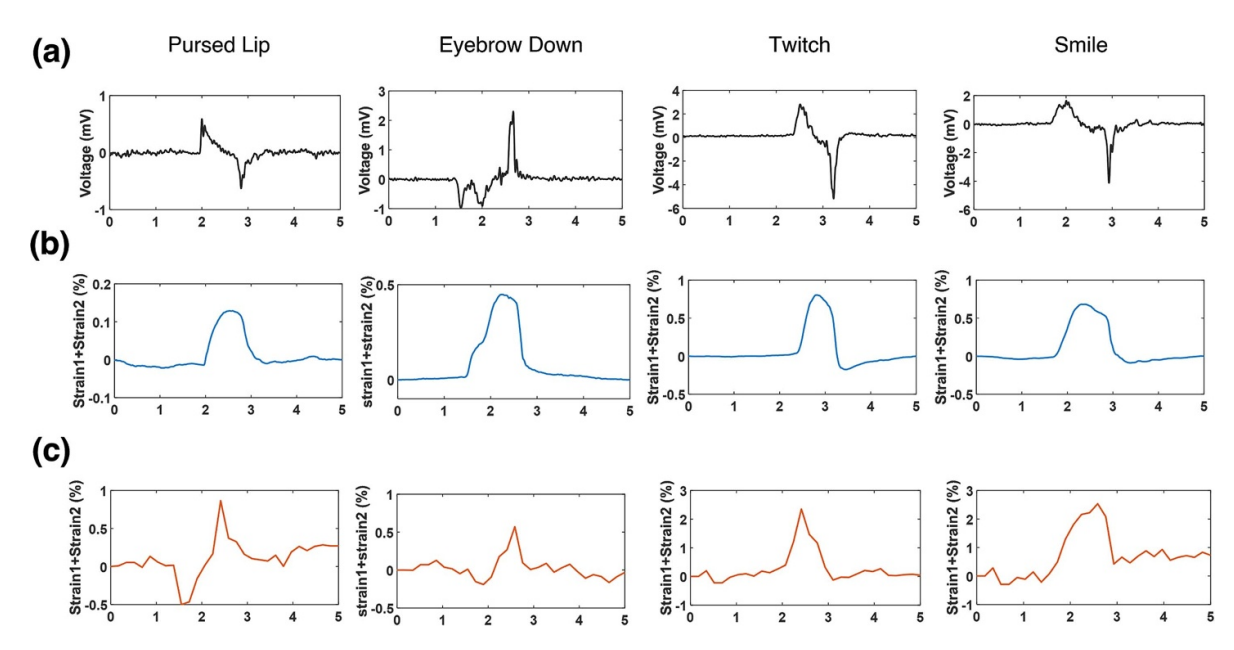


Figure 6. Four separate facial motions of 'pursed lip', 'eyebrow down', 'twitch', and 'smile' performed by a healthy subject for prediction and validation of cFaCES performance *in-vivo*, (a) experimental voltage output (black), (b) theoretical summation of principal strains (blue), (c) experimental summation of principal strains (red). All *x* axes are time in seconds.

following reasons: The experimental strains are captured from the top surface of the 3M Tegaderm tape (by which the cFaCES is adhered to the skin) by averaging the values from a mesh triangles located over the piezo elements in a strain map generated via 3D digital image correlation (DIC) (figure 7) [39, 43, 44].

If the tape is slightly displaced, the results are affected accordingly. The key fact to notice is that among multiple layers of the cFaCES sensor, most of them including the PDMS and the Tegaderm tape are orders of magnitude more flexible than the piezoelectric patches. As a result in the area of the sensor where there is no AlN patch the strain is much higher than the areas that include an AlN patch. This significant spatial variation averages out in the Tegaderm layer and causes significant variation of strain in the thickness direction. Our FEM model is instrumental in understanding this phenomenon. Figure 8 displays the strain variation along the X axis (along the length of the sensor)of the tape for the sensor under 10% uniaxial strain. The results show how the strain distribution is significantly non-uniform, and measuring the strain values slightly away from the circular elements could result in reporting higher amounts of strains. Figure 8 illustrates strain distribution under 10% uniaxial strain of the skin beneath the sensor. In figures 8(a) and (b), we observe strain values increase as moving away from circular elements and reach to its maximum value in the middle of circular elements. Figure 8(c) shows strain distribution along thickness for all layers from PDMS to top of the tape. Strain decreases from around 5% from bottom of PDMS to around 1% to top of the tape. This analysis shows that it is correct to measure larger values of strain at the surface of the Tegaderm tape compared to the strain at the AlN level. It justifies the difference between the magnitude of the strain measured by the DIC method and the strain estimated from the voltage output of the piezoelectric layer.

We further take a close look into how the strain distribution is in only the piezo layer. Figure 8(d) confirms the assumption made in the analytical model that the strain distribution in the piezoelectric layer is approximately uniform.

5. Design considerations

In this section, we use the validated FEM model to investigate the two design considerations based on minimum radius of curvature, and shape of sensing elements. In section 5.1, we evaluate the design effectiveness based on minimum radius of curvature. In section 5.2, we discuss another design with the same performance of the proposed sensor for future fabrications based on rectangular sensing elements.

5.1. Minimum radius of curvature

One of the factors to design the sensor is minimum radius of curvature to make sure the device can successfully operate on different regions of the face during bending motion. Flat areas such as the cheek and forehead have a small amount of curvature while other areas like the nose have the largest curvature [45]. The sensor should be sufficiently flexible to attach to relatively sharp areas of the face such as the nose. We designed the sensor such that the neutral mechanical plane of the system is located in the middle of piezoelectric elements; as a result, the effective strains of sensing elements are tensile at top and compressive at the bottom of the piezoelectric elements. Based on the Euler Bernoulli beam model, in bending motion the strain is calculated as

$$\epsilon = \frac{\delta}{R_c}$$

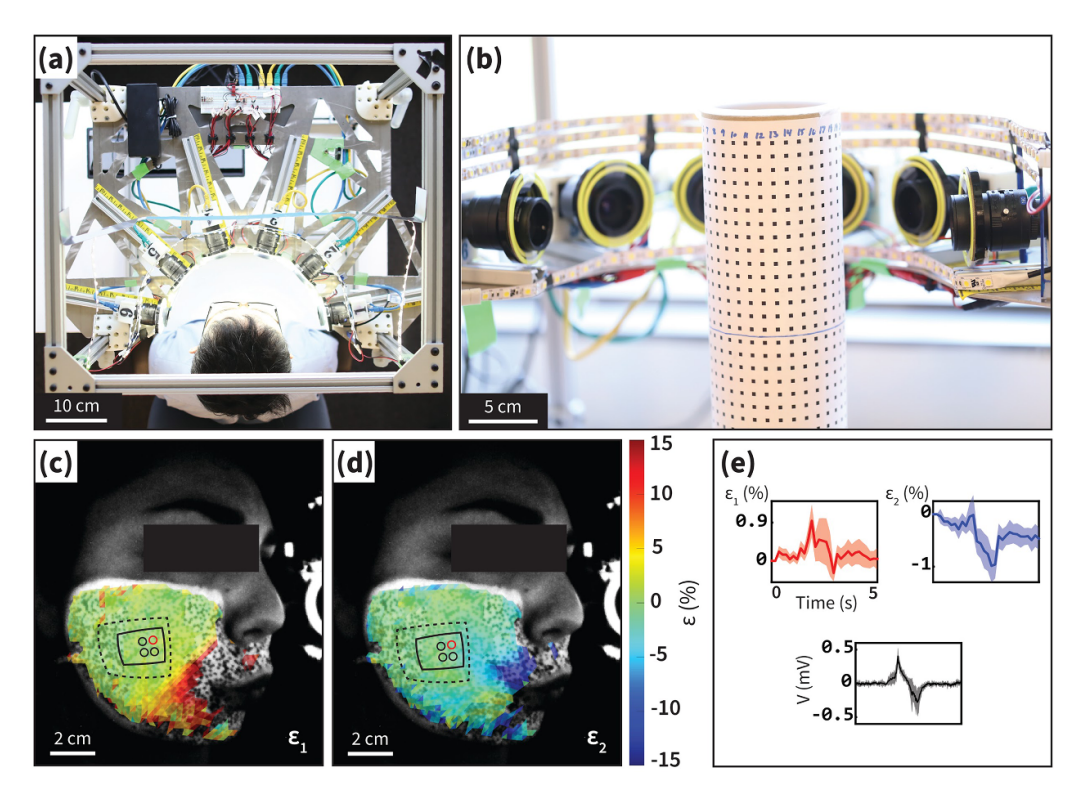


Figure 7. Overview of the experimental 3D digital image correlation (3D-DIC) system used to extract bio kinematic information from facial deformations [39]. (a) Top view of DIC setup, comprising six cameras spaced radially around the subject's face in order to get full-field image capture during natural deformations of facial skin. The cameras are connected to a network switch, which sends raw image data to a host computer (not pictured). (b) Close-up of the camera arrangement with a calibration object placed at the center of view. Ring lights around each camera lens and LED strips around the camera arrangement help to illuminate the subject of 3D-DIC. Representative 3D-DIC results for the maximal (c) and minimal (d) principal strains for a healthy subject performing the pursed lips (PL) motion while the cFaCES is laminated on the cheek (black box) with 3M Tegaderm tape (black dashed box). The circles represent the locations of the sensing elements in the cFaCES. (e) Graphs of the maximal (red) and minimal (blue) principal strains at the location of one sensing element (red circle) in (c) and (d), and the voltage generated by the same sensing element during the facial deformation.

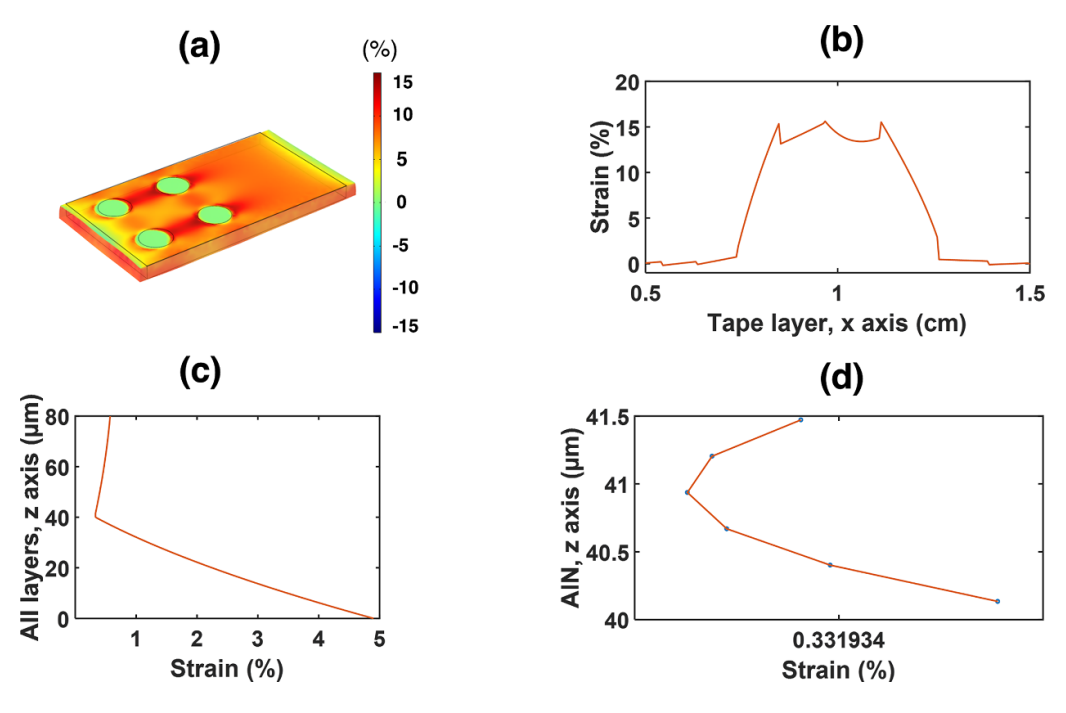


Figure 8. FEM modeling of the sensor under 10% uniaxial strain applied to the skin (a) strain distribution map, scale bar in the right shows the strain in %, (b) strain distribution over tape in X axis from center to center of circular elements, (c) strain distribution along z directions from PDMS layer to top of tape directly above center of circular elements, (d) strain distribution along AlN thickness.

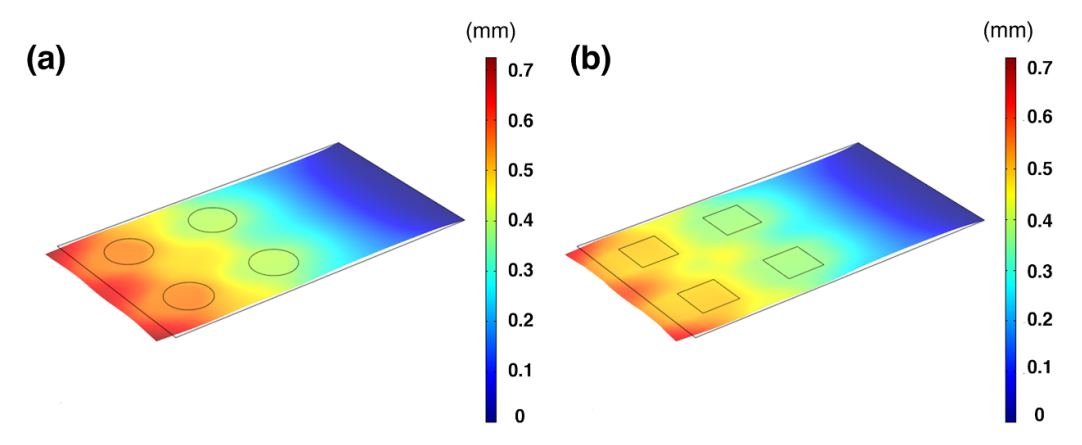


Figure 9. Displacement distribution over the length of sensor in mm under 0.1 N uniaxial stretching with (a) circular sensing elements, (b) rectangular sensing elements.

where ϵ is strain, δ is the distance of the farest point to the neutral axis, and R_c is the radius of curvature. Maximum allowable strain, ϵ , is found 0.09% [46], and half the piezo thickness is the distance of the farthest point in the piezo elements to the neutral axis $\delta = \frac{t_p}{2} = 0.75 \ \mu \text{m}$ where t_p is piezo thickness. Accordingly, the minimum radius of curvature is calculated as 834 μm which shows the device can also operate on concave areas like the nose.

5.2. Shape of sensing elements

Another factor to consider for design of the sensor is the shape of sensing elements. The results from the FEM model indicate that a sensor with square piezoelectric elements has the same stiffness as the similar sensor with rectangular piezoelectric elements if the frontal area of those two sensors are the same. Figure 9 illustrates the results of displacement profile of two sensors with circular and rectangular sensing elements under 0.1 N axial stretching. The circular elements in figure 9(a) have the radius r = 0.24 cm, and the rectangular elements in figure 9(b) have the side length of $\sqrt{\pi} * r = 0.42$ cm which results in the same area. The results in figure 9 show that both of the sensors have the same displacement field distribution which confirms that sensor stiffness is independent of the shape, and rectangular sensing elements maintaining the same lateral area could be another design to consider for future generations of sensors.

6. Parametric study and optimization based on thicknesses

There are two key design parameters to consider for optimizing the thicknesses: voltage sensitivity and compliance. The greater the voltage sensitivity, the better the performance. The second key characteristic is the mechanical compliance of the sensor. If the sensor is not mechanically compatible, i.e. of similar axial stiffness, to facial skin, the device will be uncomfortable to users and the amplitude of the facial deformations will reduce due to the absorption of energy by the stiffer-than-skin sensor. The voltage sensitivity of the sensor can be

amplified by changing the thickness in terms of its piezoelectric elements or substrate layer. At the same time, this change in thickness might have a negative impact on sensor performance by decreasing its compliance, and a trade-off exists between the two factors. In the following section, we discuss the effect of thickness on each of the design parameters, separately.

6.1. Compliance of sensor

To be conformable, the sensor is designed to have minimal bending stiffness. Therefore, the critical value for sensor compliance is its axial stiffness. If the axial stiffness is much larger than skin, it will affect the skin deformations by potentially diminishing the amplitudes of skin deformations. At the same time, the device becomes more rigid and uncomfortable to users. The axial stiffness of the skin is estimated as $k = \frac{EA}{L}$, where E is Young's modulus of the skin, A is lateral area, and L is length of skin under the sensor. The skin Young's modulus is assumed to be $E \sim 31$ kPa [47] and thickness ~ 6.39 mm [48] (this corresponds to experimental average values from cheek skin). The resulting estimated value of the stiffness of the skin is 113 N m^{-1} . We calculate the stiffness of the sensor by modeling a fully detailed model. The stiffness analysis is performed by applying a unit one-dimensional force to one end of the sensor while the other end is clamped. We measure the axial deformation of the sensor and calculate the equivalent stiffness by dividing the force by the axial displacement. The stiffness k and compliance S are defined as $k = \frac{(EA)_{\text{eff}}}{L}$, $S = \frac{1}{k}$ where E is the effective young's modulus, A is the effective area, and L is the length. The sensor moves along the x axis, and the resulting average tip displacement is evaluated as the decoupled displacement d, and the stiffness k is evaluated as $k = \frac{F}{d}$. The magnitude of the displacement along the x-axis under the implemented axial loading is 0.006 m. The current device design with 1.5 μ m thick AlN has a stiffness of 166 N m⁻¹, which shows that the stiffness of the device is close to the skin stiffness. The above model is now used to obtain the stiffness mapping relative to the piezo thickness and substrate thickness. From figure 10(a), one can intuitively view

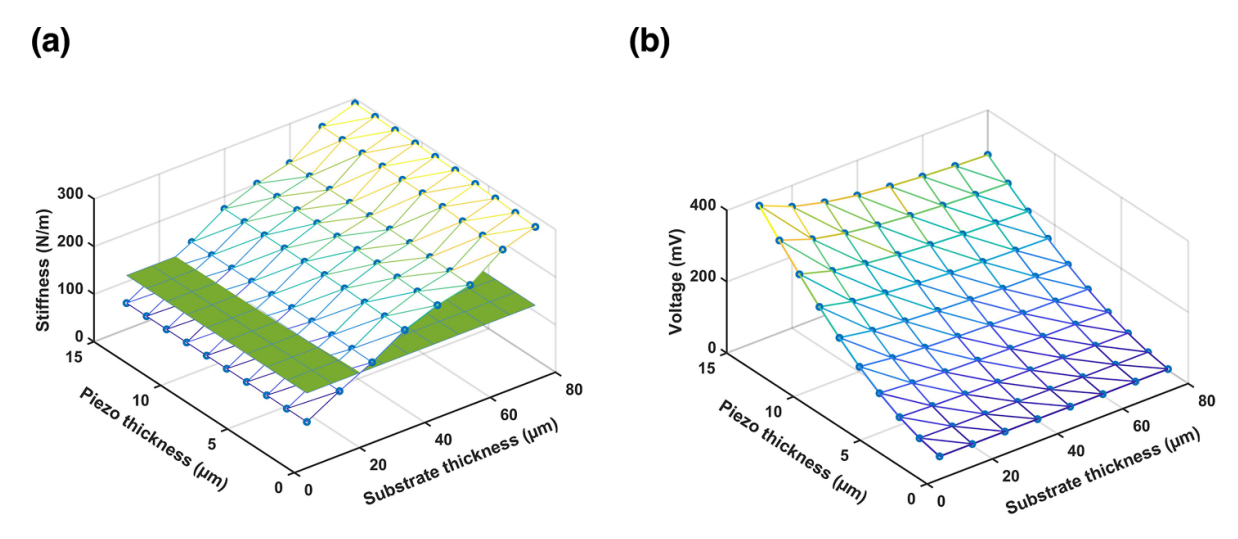


Figure 10. Effect of piezo and substrate thickness on, (a) stiffness (horizontal plane represents the facial skin stiffness, and (b) voltage generation.

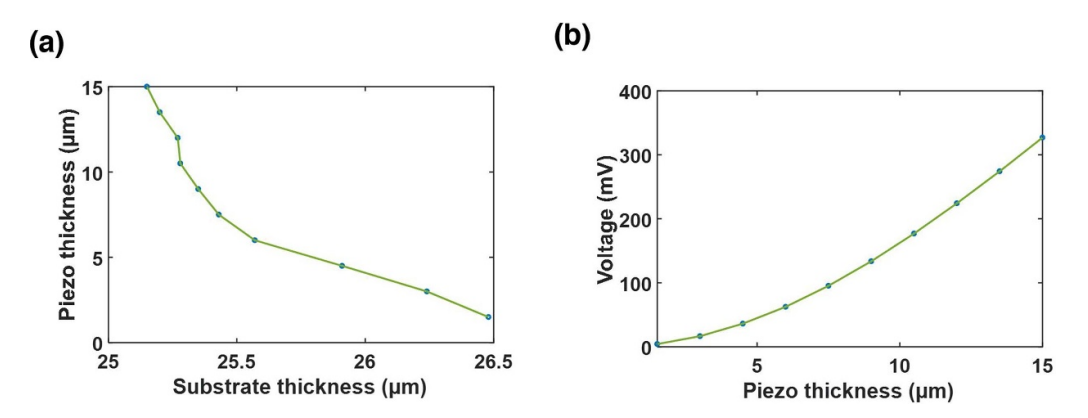


Figure 11. Graphs representing the optimum case where sensor stiffness equals facial skin stiffness, (a) piezo thickness versus substrate thickness, and (b) voltage versus piezo thickness.

the stiffness distribution and evaluate how the sensor stiffness varies with the thickness of AlN elements and the thickness of PDMS substrate. The 3D graph in figure 10(a) shows the stiffness of the sensor is more sensitive to substrate thickness than piezo thickness and the graph is inclined toward substrate thickness axis. The reason for stopping at 15 μ m thickness for AlN is attributed to the fabrication limitations. If we use thicker sensing elements, the device might be broken as well as not be ideal for comfortable usage on skin. The facial skin stiffness is illustrated as a horizontal green plane in figure 10(a). The figure 10(b) illustrates the larger the piezoelectric thickness, the larger the voltage output. On the other hand, the larger the AIN thickness the stiffer the sensor. The optimal case thus corresponds to the thickest AlN thickness that does not result in the sensor stiffness to be larger than the stiffness of the skin. The intersection of horizontal plane and inclined plane thus describes the optimum case for designing the sensor.

6.2. Voltage sensitivity of sensor

Parametric study via the FEM model is performed under an applied uniaxial strain of 1%. The average generated voltage output from sensing elements is measured for different substrate thickness and piezo thickness, and the results from parametric study are shown in figure 11(b). The 3D graph implies the device with lower substrate thickness and higher piezo thickness has higher voltage sensitivity. The smallest voltage output is 3.7 mV when the piezo thickness and substrate thickness are 1.5 μm and 80 μm , respectively, and the highest voltage output corresponds to maximum piezo thickness and minimum substrate thickness of 15 μ m and 10 μ m, respectively. The graph is inclined along piezo axis thickness which implies the generated voltage is more sensitive to piezo thickness than substrate thickness. The generated voltage drops from 5 mV to 3.7 mV by increasing the substrate thickness from 10 μ m to 80 μ m for piezo thickness of 1.5 μ m. At substrate thickness of 40 μ m, the voltage increases from 4.1 mV to 378 mV by increasing the piezo thickness from $1.5 \mu m$ to $15 \mu m$.

To find the optimal device configuration, we first find the relation between the thickness of the substrate and the AlN layers that result in the sensor having the same stiffness as the skin. We then find the best thickness of the piezoelectric layer that observes the skin stiffness constraint. The line in

figure 11(b) is the intersection of horizontal plane and inclined plane in figure 10(a) meaning the sensor stiffness and the skin stiffness are the same. As expected, if we increase the thickness of the AlN layer we must decrease the thickness of the substrate to compensate for the added stiffness. By changing the thickness of the piezoelectric layer we can identify the optimal thickness that results in the maximum voltage. The voltage output related to optimum thicknesses is illustrated in figure 11(b) which shows an increase from 4.3 mV to 326.9 mV by increasing the piezo thickness from 1.5 μ m and 15 μ m.

7. Conclusion

In this paper, we present the development of a finite element model for simulations of a conformable piezoelectric sensor. The developed model was experimentally verified through a set of in vitro dynamic mechanical tests under bending, stretching, and compression as well as in vivo experiments on healthy and amyotrophic lateral sclerosis (ALS) subjects. The strain distribution in different layers of the cFaCES is evaluated to better understand in vivo experiments. The validated model was further extended to the design and optimization of the device. The analysis of the design shows the device satisfies the radius of curvature requirements and could operate on different regions of face. Parametric studies show that voltage sensitivity and compliance of the sensor were sensitive to geometric properties like thickness of layers. Voltage sensitivity was mostly affected by thickness of piezo elements, however; sensor compliance considerably changes with substrate thickness. The optimum value of substrate and piezo thicknesses were assessed through facial skin stiffness value. The cFaCES has the same stiffness as facial skin for substrate thickness of 26.5 μ m and piezo thickness of 1.5 μ m.

Data availability statement

All data is available in the main text or supplementary materials. All data and materials used in the analysis are available in some form to any researcher for purposes of reproducing or extending the analysis, upon the request from the corresponding author.

The data that support the findings of this study are openly available at the following URL/DOI: www.zenodo.org.

Acknowledgments

M A K thanks the National Institute of Biomedical Imaging and Bioengineering of the National Institutes of Health under award number R21EB023613 by which the research reported in this publication was partially supported. M A K also thanks the National Science Foundation under Grant No. 1905252 to partially support this work. C D acknowledges that the experimental part of this research was supported by MIT Media Lab Consortium and NSF ECCS Award Number (FAIN): 2026344. The authors thank Dr Tao Sun, former

research scientist at MIT Media Lab, for helping to recruit experimental tests. C D, and F T thank Dr Robert Brown of the University of Massachusetts Medical School for helping to recruit the ALS patients and fruitful discussion on cFaCES application on the ALS subjects. The authors thank the families of Phyl Gerber and Dennis Ceruti for their generous help and profound dedication in ALS patient trials. The authors also acknowledge the microfabrication facility/cleanroom of Conformable Decoders research group at the MIT Media Lab, the YellowBox, as well as the Instron Lab of Koch Institute For Integrative Cancer Research at MIT. Funding: The research was supported by MIT Media Lab Consortium funding. This work was performed in part at the Center for Nanoscale Systems (CNS), a member of the National Nanotechnology Coordinated Infrastructure Network (NNCI), which was supported by the National Science Foundation under NSF Award No. 1541959. CNS is part of Harvard University.

Author contributions

A K and C D conceived the overall research goals and aims. F T, and C D designed and conducted all experiments. N A, M T A, and M A K conducted all theoretical calculations and FEM. All authors contributed to the manuscript writing.

Conflict of interest

The authors declare no competing interests.

Code availability

All code used in the analysis is available to any researcher for purposes of reproducing or extending the analysis, upon the request from the corresponding author.

Conflict of interest

The authors declare that there is no conflict of interest.

ORCID iDs

Canan Dagdeviren https://orcid.org/0000-0002-2032-792x

M Amin Karami https://orcid.org/0000-0001-9882-8807

References

- [1] Tasnim F et al 2018 Foresight 20 589
- [2] Dagdeviren C, Li Z and Wang Z L 2017 Annu. Rev. Biomed. Eng. 19 85
- [3] Dagdeviren C, Joe P, Tuzman O L, Park K-I, Lee K J, Shi Y, Huang Y and Rogers J A 2016 Extreme Mech. Lett. 9 269
- [4] Dagdeviren C et al 2015 Nat. Mater. 14 728
- [5] Yuan J, Dagdeviren C, Shi Y, Ma Y, Feng X, Rogers J A and Huang Y 2016 Proc. Math. Phys. Eng. Sci. 472 20160225
- [6] Shi Y, Dagdeviren C, Rogers J A, Gao C F and Huang Y 2015 J. Appl. Mech. 82

- [7] Yuan J H, Shi Y, Pharr M, Feng X, Rogers J A and Huang Y 2016 J. Appl. Mech. 83 0845011
- [8] Park S-H, Lee H B, Yeon S M, Park J and Lee N K 2016 ACS Appl. Mater. Interfaces 8 24773
- [9] Yoon S, Sim J K and Cho Y-H 2016 *Sci. Rep.* **6** 23468
- [10] Wang X, Song W-Z, You M-H, Zhang J, Yu M, Fan Z, Ramakrishna S and Long Y-Z 2018 ACS Nano 12 8588
- [11] Viola F A, Spanu A, Ricci P C, Bonfiglio A and Cosseddu P 2018 Sci. Rep. 8 8073
- [12] Yoon S and Cho Y-H 2014 J. Phys. Conf. Ser. 557 012026
- [13] Ansari M H and Karami M A 2018 J. Intell. Mater. Syst. Struct. 29 438
- [14] Ansari M H and Karami M A 2017 *Smart Mater. Struct.* **26** 065001
- [15] Ansari M H and Karami M A 2016 J. Appl. Phys. 119 094506
- [16] Avirovik D, Karami M A, Inman D and Priya S 2012 IEEE Trans. Ultrason. Ferroelectr. Freq. Control 59 108
- [17] American Society of Mechanical Engineers Digital Collection n.d. Volumes | Smart Materials, Adaptive Structures and Intelligent Systems (available at: https://asmedigital collection.asme.org/SMASIS/SMASIS2018/volume/ 51951)
- [18] Bani-Hani M, Amin Karami M, Amiri N and Anbarani M T 2018 Volume 2: Mechanics and Behavior of Active Materials; Structural Health Monitoring; Bioinspired Smart Materials and Systems; Energy Harvesting; Emerging Technologies (https://doi.org/10.1115/smasis2018-8199)
- [19] Amin Karami M and Inman D J 2012 Appl. Phys. Lett. 100 042901
- [20] Nanda A and Amin Karami M 2017 Volume 2: Modeling, Simulation and Control of Adaptive Systems; Integrated System Design and Implementation; Structural Health Monitoring (https://doi.org/10.1115/smasis2017-3892)
- [21] Nanda A and Karami M A 2017 J. Appl. Phys. 121 124506
- [22] Nanda A and Karami M A 2018 J. Acoust. Soc. Am. 144 412
- [23] Dagdeviren C et al 2014 Nat. Commun. 5 4496
- [24] Yang Y, Tang L and Li H 2009 Smart Mater. Struct. 18 115025
- [25] Song H J, Choi Y-T, Wereley N M and Purekar A S 2010 J. Intell. Mater. Syst. Struct. 21 647
- [26] Williams R B, Inman D J and Wilkie W K 2006 J. Intell. Mater. Syst. Struct. 17 601
- [27] Biscani F, Nasser H, Belouettar S and Carrera E 2011 Composites B 42 444
- [28] Bilgen O, Kochersberger K B, Inman D J and Ohanian O J III 2010 Smart Mater. Struct. 19 055010
- [29] Bilgen O, Friswell M, Kochersberger K and Inman D 2011 52nd AIAA/ASME/ASCE/AHS/ASC Structures, Structural

- *Dynamics and Materials Conf.* (American Institute Of Aeronautics And Astronautics) (https://doi.org/10.2514/6.2011-2072)
- [30] Sodano H A, Park G and Inman D J 2004 Mech. Syst. Signal Process. 18 683
- [31] Nagata Y, Park S and Ming A 2006 2006 IEEE Int. Conf. on Robotics and Biomimetics pp 1275–80
- [32] Kuang Y and Zhu M 2019 Composites B 158 189
- [33] Trindade M A and Benjeddou A 2012 Acta Mechanica 34 352
- [34] Nováková K and Mokrý P 2011 2011 10th Int. Workshop on Electronics, Control, Measurement and Signals pp 1–5
- [35] Nguyen V-T, Kumar P and Leong J Y C 2018 Computation 6 60
- [36] Feng X, Yang B D, Liu Y, Wang Y, Dagdeviren C, Liu Z, Carlson A, Li J, Huang Y and Rogers J A 2011 ACS Nano 5 3326
- [37] Duan Y, Huang Y, Yin Z, Bu N and Dong W 2014 Nanoscale 6 3289
- [38] Murat Koç I and Akça E 2013 Tribol. Int. 59 321
- [39] Sun T, Tasnim F, McIntosh R, Amiri N, Solav D, Anbarani M, Sadat D, Zhang L, Gu Y and Amin Karami M 2020 Decoding of facial strains via conformable piezoelectric interfaces *Nature Biomedical Engineering* (https://doi.org/10.1038/s41551-020-00612-w)
- [40] Kyrgiazoglou A and Theodoulidis T 2017 Simulation of Eddy Current Non Destructive Testing using COMSOL®
 Multiphysics COMSOL MULTIPHYSICS CONFERENCE
 Proc. COMSOL Conf. (Rotterdam) 2017 Rotterdam,
 Netherlands (https://www.researchgate.net/publication/
 323512416_Simulation_of_Eddy_Current_Non_
 Destructive_Testing_using_COMSOLR_Multiphysics)
- [41] Leo D J 2007 Engineering Analysis of Smart Material Systems (New York: Wiley) p 576 (https://www.wiley.com/en-us/ Engineering+Analysis+of+Smart+Material+Systems+-p-9780471684770)
- [42] Preumont A 2006 Mechatronics—Dynamics of Electromechanical and Piezoelectric Systems (Berlin: Springer) (https://www.springer.com/gp/book/ 9781402046957)
- [43] Solav D, Moerman K M, Jaeger A M, Genovese K and Herr H M 2018 *IEEE Access* 6 30520
- [44] Solav D, Moerman K M, Jaeger A M and Herr H 2019 IEEE Trans. Biomed. Eng. (https://doi.org/10.1109/TBME. 2019.2895283)
- [45] Tsagkrasoulis D, Hysi P, Spector T and Montana G 2017 Sci. Rep. 7 45885
- [46] Zhao Y, Peng X, Fu T, Huang C, Xiang H, Hu N and Yan C 2018 Materialia 2 148
- [47] Luboz V, Promayon E and Payan Y 2014 Ann. Biomed. Eng. 42 2369
- [48] Kim Y-S, Lee K-W, Kim J-S, Gil Y-C, Tanvaa T, Shin D H and Kim H-J 2019 Clin. Anat. 32 1008